https://doi.org/10.31436/iiumej.v27i3.3191

Optimization of Interdigitated Electrode through Finite Element Analysis for Juice Adulteration Detection

SAKINAH ABDUL HAMID[1], MOHD ASYRAF MOHD RAZIB[1,2*], MARMEEZEE MOHD YUSOFF[1]

[1]*Department of Mechatronic Engineering, Kulliyyah of Engineering, International Islamic University of Malaysia, Jalan Gombak, 53100 Kuala Lumpur, Malaysia*
[2]*VLSI-MEMS Research Unit, Department of Electrical and Computer Engineering, Kulliyyah of Engineering, International Islamic University of Malaysia, Jalan Gombak, 53100 Kuala Lumpur, Malaysia*

**Corresponding author: asyrafr@iium.edu.my*

(Received: 02 April 2024; Accepted: 6 August 2026; Published online: 11 September 2026)

ABSTRACT: Recently, interdigitated electrodes (IDEs) have been applied in various industries because they are easy to fabricate and low-cost. However, the optimal electrode geometry for maximizing sensitivity remains unclear, as conflicting reports exist on the effects of finger width, spacing, and thickness under varying operating conditions. Therefore, a simulation study was conducted using COMSOL Multiphysics 5.6 software to determine which IDE offers the best sensitivity. The IDEs operate with two parallel coplanar electrodes, with periodic repetition of the design (i.e., length, width, and electrode spacing) to generate a high signal and reduce the signal-to-noise ratio. Finite element analysis via COMSOL revealed that an optimized configuration featuring a smaller gap size (0.1 mm), a wider finger width (0.4 mm), and an electrode count of 8 yielded an ideal sensor design, achieving a peak electric field of 2582.52 V/m and a current density of 1.57×10^{10} A/m^2. Following the computational analysis, the optimized IDE sensor was physically fabricated. Experimental verification using this low-cost, screen-printed silver sensor successfully demonstrated a distinct contrast in electrical resistance; pure fruit juices exhibited a low baseline resistance between 2.5 and 6 Ω, whereas commercialized variants reached significantly higher values of up to 35 Ω over a 5-hour testing window. This strong correlation highlights the platform's stability and its immediate capacity to distinguish juice purity. These findings confirm that the optimized IDE platform provides a highly viable, inexpensive solution for detecting food and beverage adulteration.

ABSTRAK: Kebelakangan ini, elektrod berselang-seli (IDE) telah digunakan secara meluas dalam pelbagai industri kerana mudah difabrikasi dan berkos rendah. Walau bagaimanapun, geometri elektrod yang optimum bagi memaksimum kepekaan masih tidak jelas, kerana terdapat laporan bercanggah mengenai kesan lebar jari, jarak, dan ketebalan di bawah keadaan operasi berbeza. Oleh itu, satu kajian simulasi telah dijalankan menggunakan perisian COMSOL Multiphysics 5.6 bagi menentukan konfigurasi IDE berkepekaan terbaik. IDE beroperasi berdasarkan dua elektrod koplanar selari, dengan pengulangan berkala parameter reka bentuk iaitu panjang, lebar, dan jarak antara elektrod, bagi menjana isyarat tertinggi dan mengurangkan nisbah isyarat-ke-bunyi. Analisis unsur terhingga melalui COMSOL mendapati bahawa konfigurasi optimum dengan saiz jurang ebih kecil (0.1 mm), lebar jari lebih lebar (0.4 mm), dan bilangan elektrod sebanyak 8 telah menghasilkan reka bentuk sensor ideal, dengan mencapai medan elektrik puncak sebanyak 2582.52 V/m dan ketumpatan arus sebanyak 1.57×10^{10} A/m². Selepas analisis pengiraan, sensor IDE yang dioptimumkan telah difabrikasi secara fizikal. Pengesahan eksperimen menggunakan sensor perak cetakan skrin berkos rendah ini berjaya menunjukkan perbezaan ketara dalam rintangan elektrik; jus buah-

buahan tulen menunjukkan rintangan asas yang rendah antara 2.5 Ω dan 6 Ω, manakala varian komersial mencapai nilai yang lebih tinggi sehingga 35 Ω dalam tempoh ujian selama 5 jam. Korelasi yang kuat ini menyerlahkan kestabilan platform dan keupayaannya yang segera bagi membezakan ketulenan jus. Penemuan ini mengesahkan bahawa platform IDE yang dioptimumkan menyediakan penyelesaian praktikal dan murah bagi mengesan pemalsuan makanan dan minuman.

KEYWORDS: *Interdigitated electrode (IDE), Finite Element Analysis, Biosensor*

1. INTRODUCTION

Interdigitated Electrodes (IDEs) are universal transducers in modern technologies that fall under the category of electrochemical biosensors featuring micro- or nanoscale terminal arrays [1]. These biosensors can be readily integrated into mobile lab-on-chip devices, enabling rapid point-of-care diagnosis. Compared with other impedimetric biosensing configurations, this architecture offers excellent sensitivity, low cost, and ease of fabrication, which are the primary advantages of these sensors [2]. Furthermore, IDEs eliminate the operational requirement for a reference electrode while providing a straightforward methodology for obtaining a steady-state current response. Consequently, such sensors have been widely utilized to monitor capacitance, impedance, dielectric constant, and mass conductivity in biological and chemical media [3].

Sensing devices utilizing IDEs can operate in either faradaic or non-faradaic modes. The distinction between faradaic and non-faradaic processes is essential for characterizing sensor performance. A faradaic process is fundamentally governed by transient electron transfer across the electrode-electrolyte interface via chemical oxidation and reduction reactions, whereas non-faradaic modes rely on changes in capacitance such as double-layer capacitance and physical molecular binding events at the electrode surface without charge transfer [4]. When implementing capacitive or impedimetric sensors, IDEs offer an exceptionally effective planar structure. Conventionally, an IDE has a coplanar architecture composed of two individually addressable, comb-like electrode structures that form a precise gap between them. In these configurations, fringe or edge field effects become less dominant when the finger-length dimensions significantly exceed the electrode layer thickness [5].

Mathematical modeling and finite element simulation are essential engineering tools before physical fabrication, as they minimize the time and cost of prototyping. Recent studies have demonstrated the effectiveness of finite element analysis in optimizing IDE performance by evaluating the influence of key parameters such as gap size, finger width, and electrode count on sensor sensitivity [6]. Furthermore, modeling enables a deeper evaluation of system physics under varying operational constraints, providing a clear pathway for design optimization. To this end, this study aims to optimize the geometric configuration of an IDE sensor via finite element analysis to achieve maximum sensitivity, followed by physical realization using a cost-effective manufacturing route. This work systematically evaluates the influence of gap size, finger width, electrode count, and material types on localized electric-field distribution and current-density profiles. By translating optimized simulation topologies into actual, flexible silver-paste electrodes screen-printed onto polyethylene terephthalate (PET) substrates, this study demonstrates a scalable framework for rapid, portable beverage quality assurance. Ultimately, this work provides an affordable, high-sensitivity electrochemical testing platform capable of robustly distinguishing pure fruit juices from commercialized or adulterated alternatives, addressing a critical need for accessible quality control in the beverage industry [7].

2. METHODOLOGY

2.1. Biosensor Structure

An IDE is a coplanar structure composed of two individually addressable interdigitated combs that form a micro-sized gap between them, as shown in Fig. 1. The comb-like structure is a convenient, simple, and low-cost design that can be used in a variety of applications [8]. IDEs operate based on two parallel-plate capacitors and a sample under test. Capacitance describes how two conductive objects separated by a space respond to a voltage difference applied to them. An electric field is established between them, causing positive and negative charges to collect on each object. In IDEs, the term "interdigit" refers to the repeated coplanar, digit-like or finger-like pattern used to generate a high signal and reduce the signal-to-noise ratio [9, 10]. The three major measurement concepts are changes in dielectric properties, charge distribution, and conductivity when the analyte forms on the IDE surface.

Fig. 1 shows the structure of the IDE, in which one plate serves as the ground (negative terminal). In contrast, the other serves as the electric potential (positive terminal), to which an alternating current (AC) voltage signal is applied to create an electric field between these two terminals [11]. The individual electrode finger width is defined as W_f, which is separated by a specific gap distance, G, from the opposing electrode finger. The total number of alternating finger structures across the active sensing area constitutes the electrode count parameter, N. Fig. 1 shows all parameters. Any medium placed on the sensors increases the electric potential, creating an electric field above the sensor that penetrates the sample under test [12].

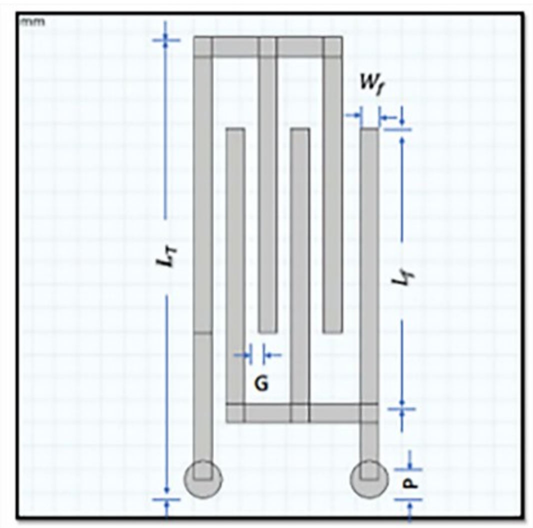

Figure 1. IDE geometry parameters

2.2. Finite Element Simulation

The IDE structure is simulated using COMSOL Multiphysics version 5.6 to investigate the electric field distribution and current density for the proposed parameters [13]. COMSOL is a software platform used to model and simulate multiphysics applications using advanced numerical methods. The simulation results help distinguish the effects of the electric field for various parameters and determine which design is best for this project.

The performance of the IDE's geometrical parameters is evaluated by analyzing electric-field strength and current-density flow. Various IDE geometric layouts are designed in 2D. The electric-field strength generated by the capacitive sensor is a key factor in evaluating sensitivity performance. To perform numerical calculations of electric fields, AC and DC modules need to be simulated [14]. The working and counter electrodes were simulated with different geometries, such as width, thickness, and electrode gap. The electric field will be generated between the working and ground electrodes [15]. The Ohm's law will be used to begin the numerical calculation as Eq. (1) where J is the current density, σ is the conductivity of DMEM, E is the electric field, D is the electric displacement, and Je is the external current density.

$$J = \sigma E + jwD + Je \tag{1}$$

The electric field (E) and electric displacement (D) were obtained from the gradient of voltage (V) at each static point, as in Eq. (2) and Eq. (3), where ε_0 and ε_r are the permittivity of free space and the permittivity of the electrode, respectively. The equation used for numerically calculating the electrode spacing and capacitance is Eq. (4), where C is the capacitance of the IDE structure, A is the area of the surface sensor, and d is the distance between the electrodes.

$$E = -\nabla V \tag{2}$$

$$D = \varepsilon_0 \varepsilon_r E \tag{3}$$

$$C = \varepsilon_0 \varepsilon_r \frac{A}{d} \tag{4}$$

In this study, four simulations are being performed: the gap size between the electrodes, the width of the fingers, the number of electrodes, and the material used. The first simulation involves adjusting the gap between the electrodes from 0.1 mm to 0.5 mm (increasing by 0.1 mm each time). The relationship between finger width and performance varied from 0.2 mm to 0.4 mm (increasing by 0.05 mm each time). The simulation then increased the number of fingers from four to twelve (increasing by two fingers each time). The final simulation will test silver (Ag), gold (Au), and platinum (Pt) substrate materials. Table 1 shows the geometry parameters of the IDEs simulated in this study.

Table 1. IDE Design Parameters

Parameter	Symbol	Values	Unit
Total IDE Length	L_T	10.0	mm
Padding Size	P	$\pi * 0.4^2$	mm^2
Gap between Fingers	G	0.1 – 0.5	mm
Finger Width	W_f	0.2 – 0.4	mm
Number of Fingers	N	4 -12 fingers	
Finger Length	L_f	6	mm

The sequential optimization workflow, proceeding from electrode gap size (G), to finger width (W_f), electrode finger numbers (N), and finally electrode material selection, was deliberately structured based on a physics-driven hierarchy of parameter dominance. The local electric field intensity (E) and primary charge transport dynamics are most sensitively governed by the immediate spatial proximity between opposing conductors (G), as dictated by the electrostatic field gradient ($E = -\nabla V$) [16]. Once the critical field-generating gap was established, the electrode width (W_f) was optimized to maximize the active surface area and current density vectors [17]. Following these micro-scale boundary configurations, the macro-scale structural parameter (N) was evaluated to optimize total capacitance and signal-to-noise ratio within the physical footprint constraints. Finally, material types were assessed as a secondary factor to balance processing stability and electrical performance. This sequence approach ensures that primary local-field behaviors are stabilized before secondary-scale parameters are tuned.

https://doi.org/10.31436/iiumej.v27i3.3191

2.2.1. Computational Preprocessing and Boundary Conditions

To execute the numerical physics calculations, the following preprocessing parameters and boundary settings were established within the COMSOL Multiphysics environment. For the physics interface, the Electrostatics (es) and Electric Currents (ec) interfaces within the AC/DC module were utilized to resolve the domain equations [18]. For boundary conditions, a terminal voltage of 1 V ($V_0 = 1$ V) was applied as a Dirichlet boundary condition to the working electrode terminal array. The opposing counter electrode array was assigned a ground boundary condition ($V = 0$ V). All outer boundaries of the surrounding computational domain matrix were set to Charge Conservation with Zero Charge/Electric Insulation constraints. For material properties, the electrodes were modeled using the bulk electrical conductivities and isotropic relative permittivities (ε_r) corresponding to silver (Ag), gold (Au), and platinum (Pt) domains. The fluid medium domain filling the electrode gaps was assigned the material properties of the target juice matrix with predefined baseline electrical conductivities (σ) and relative dielectric constants. Lastly, a physics-controlled, triangular finite element mesh sequence was implemented. To ensure accurate convergence and capture extreme field gradients, localized mesh refinement was enforced along all sharp boundaries, fingertips, and inter-electrode gap spaces (G), yielding a highly dense grid configuration within the active sensing area.

For boundary conditions, a terminal voltage of 1 V ($V_0 = 1$ V) was applied as a Dirichlet boundary condition to the working electrode terminal array. The opposing counter electrode array was assigned a ground boundary condition ($V = 0$ V). All outer boundaries of the surrounding computational domain matrix were set to Charge Conservation with Zero Charge/Electric Insulation constraints. For material properties, the electrodes were modeled using the bulk electrical conductivities and isotropic relative permittivities (ε_r) corresponding to silver (Ag), gold (Au), and platinum (Pt) domains. The fluid medium domain filling the electrode gaps was assigned the material properties of the target juice matrix with predefined baseline electrical conductivities (σ) and relative dielectric constants. Lastly, a physics-controlled, triangular finite element mesh sequence was implemented. To ensure accurate convergence and capture extreme field gradients, localized mesh refinement was enforced along all sharp boundaries, fingertips, and inter-electrode gap spaces (G), yielding a highly dense grid configuration within the active sensing area.

2.3. Fabrication of Interdigitated Electrode (IDE) sensor.

Screen printing appeared to be the least expensive technique compared to other printing methods. The mesh with an interdigitated layout is used to transfer silver paste onto the substrate, polyethylene terephthalate (PET), as shown in Fig. 2(a). A squeegee is moved across the screen to fill the open mesh apertures with ink. Lift the mesh quickly to avoid excessive ink absorption. To achieve the optimum curing time for the ink, the printed electrodes will need to cure for 15 minutes in the oven at 80°C temperatures. The physically realized, low-cost silver IDE sensor arrays resulting from this fabrication workflow are displayed in Fig. 2(b).

The experimental testing involved four distinct samples: pure orange juice, commercial orange juice, pure apple juice, and commercial apple juice. For each test, a 1 mL droplet was precisely dispensed onto the fabricated device via a microsyringe, after which an LCR meter measured the resulting resistance and conductance.

https://doi.org/10.31436/iiumej.v27i3.3191

(a) (b)

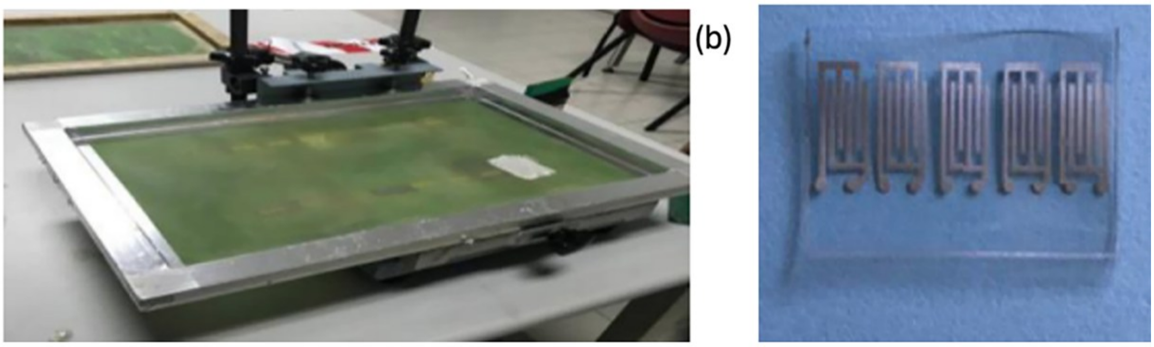

Figure 2. a) Silver ink absorbs onto the substrate through a mesh. b) Screen-printed silver interdigitated electrode (IDE) sensor chips on flexible PET substrates prior to fluid testing.

3. RESULT AND DISCUSSION

Fig. 3 depicts the colormap of the electric field and current density distribution, along with the electric field direction, for the IDE sensor design simulated in COMSOL Multiphysics. The simulation results are based on four research variables: electrode gap size, finger width, number of electrodes, and material type.

The standard unit of the electric field is the volt per meter (V/m). The electric field between the working and counter electrodes is excited when a DC voltage is applied to the working electrode. A direct spatial correlation is observed between the maximum electric field norm and the peak current density. The highest values for both parameters are concentrated along the vertical edges and sharp corners of the interdigitated fingers, particularly within the narrow gaps separating the opposing electrodes (ranging from $y = 0$ mm to $y = 4.5$ mm). As shown in Fig. 3 (left), the electric field norm peaks significantly at approximately 5×10^3 V/m at the tips and localized sharp boundaries of the inner finger channels. This intense localized field drives charge transport. Correspondingly, Fig. 3 (right) reveals that the current density norm reaches its maximum of roughly 3.5×10^{11} A/m^2 precisely within these high-field channels. The arrow surface plots confirm that the current density vectors are densely packed and tightly confined within the high-field gaps, indicating that the primary conductive pathways are restricted to these regions. Conversely, the peripheral areas, the outer boundary of the substrate, and the regions surrounding the bottom contact pads display both a negligible electric field (~ 0 V/m) and a minimal current density (~ 0 A/m^2). This confirms excellent signal confinement to the active interdigitated area with virtually no parasitic leakage current in the surrounding matrix.

The primary current pathways are strictly confined to the narrow vertical channels between the interdigitated electrode fingers. The current density arrows (Fig. 3, right) demonstrate that charge transport flows laterally across the gaps from the high-potential fingers to the grounded fingers [19]. Negligible current flows through the bulk substrate or the outer margins, indicating excellent geometric confinement of the electrical signal. Severe electric field concentrations (hotspots) are observed at the sharp corners and tips of the interdigitated fingers, as well as along the innermost vertical interfaces. The tight confinement of current density to the finger gaps maximizes the device's sensitivity and active-area utilization. However, intense localized electric-field gradients increase the risk of localized dielectric breakdown or arcing across the gaps if the operational voltage exceeds design thresholds.

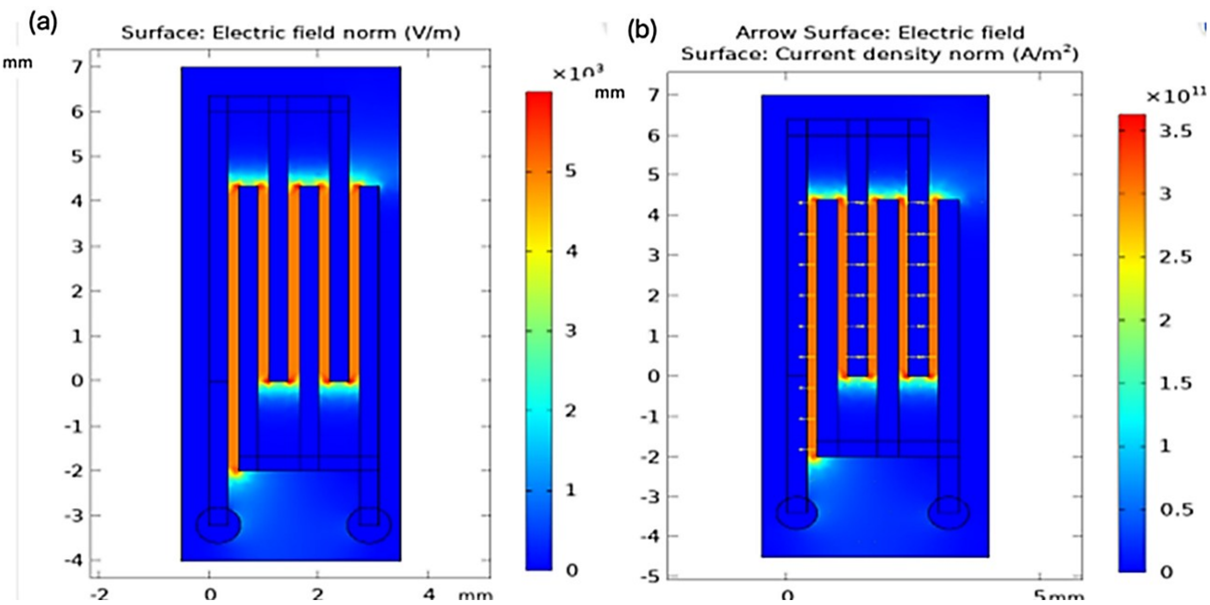

Figure 3. a) Color map of the electric field distribution of IDE. b) Color map of the current density of IDE.

3.1. Dependence on the gap between electrodes

Table 2 summarizes the calculated averages of the current density and the electric field magnitude across varying inter-electrode spacing gaps. As illustrated by the parameter trends in Fig. 4, expanding the gap size from 0.1 mm to 0.5 mm induces a dramatic, non-linear degradation in the average current density. This inverse relationship highlights that a larger spatial gap limits charge transport across the channels. Specifically, the maximum current density is achieved at the minimum evaluated gap of 0.1 mm, yielding a peak value of 1.82×10^{11} A/m^2, whereas the lowest current density drops sharply to 5.34×10^{10} A/m^2 at a gap of 0.5 mm.

Concurrently, the average electric field magnitude drops steeply as the finger spacing increases. The minimum electric field intensity of 866.87 V/m is recorded at the largest gap size of 0.5 mm, while the 0.1 mm spacing produces the maximum electric field of 2295.94 V/m. This pronounced field enhancement at smaller gaps is governed by electrostatic field-scaling laws: narrowing the conductor boundaries concentrates the potential drop, intensifying local flux lines [20]. Consequently, the IDE topology featuring a 0.1 mm gap represents the optimal design configuration, providing the maximum localized field intensity and current throughput required to maximize electrochemical sensing sensitivity. Based on these performance advantages, the 0.1 mm gap configuration was selected as the fixed baseline framework for all subsequent optimization stages.

Table 2. The average current density of various gap sizes

Gap size between fingers (mm)	Average Current Density (A/m^2)	Average Electric Field (V/m)
0.1	1.82×10^{11}	2295.94
0.2	1.46×10^{11}	1372.10
0.3	8.74×10^{11}	966.15
0.4	6.17×10^{11}	953.5
0.5	5.34×10^{11}	866.87

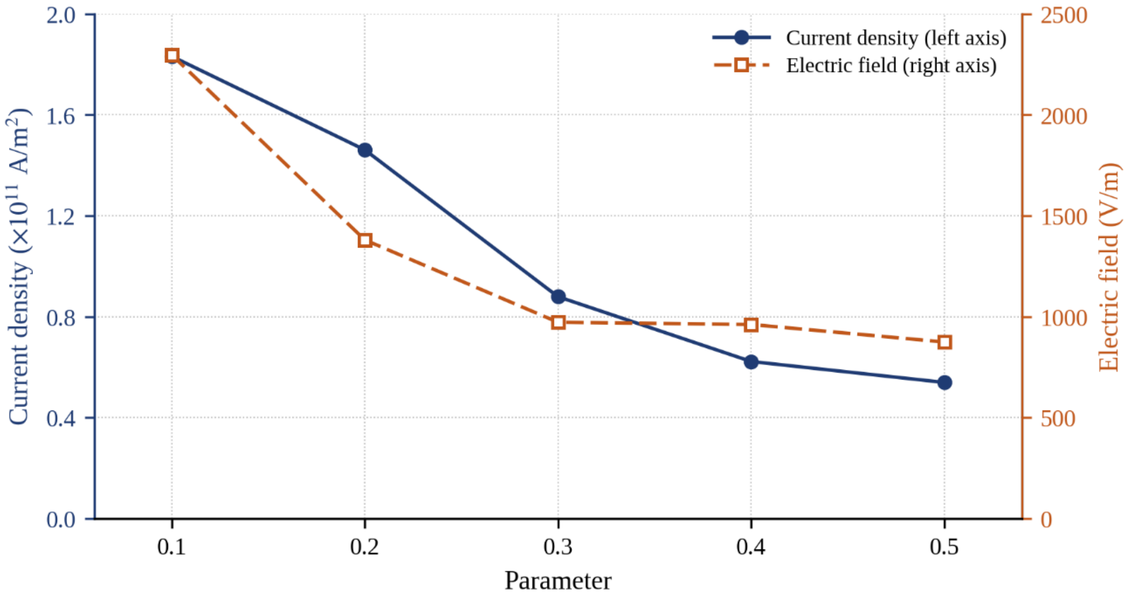

Figure 4. Graph of the average current density and electric field by varying gap sizes.

3.2. Dependence on the width of fingers

The average current density and electric field for IDEs with varying finger widths are presented in Table 3. Overall, the average current density distribution exhibits a gradual increasing trend from the smallest width (0.2 mm) to the largest width (0.4 mm), as demonstrated in Fig. 5. In this simulation, the 0.4 mm width yielded the highest current density value, indicating that wider fingers enhance charge transport efficiency. This behavior can be attributed to the increased electrode surface area available for charge accumulation and electron transfer, which facilitates higher current throughput [21].

The average electric field magnitude as a function of finger width is shown in Fig. 5. Overall, the electric field magnitude increases significantly with increasing electrode width. The highest average electric field of 2468.9 V/m was recorded at 0.4 mm, while the lowest value of 1371.53 V/m was observed at 0.2 mm. This trend follows electrostatic field-scaling principles: wider electrodes provide larger conductive surfaces for charge accumulation, intensifying the potential gradient and local flux lines. Ismail et al. [21] similarly reported that increasing electrode dimensions enhances electric field distribution and penetration depth in interdigitated electrode systems.

Thus, in the second parametric study, the 0.4 mm finger width was identified as the optimal configuration, producing both the highest current density and electric field magnitude. Consequently, this width was selected as the fixed baseline for subsequent simulation studies.

Table 3. The average current density of varying finger widths

Width of fingers (mm)	Average Current Density (A/m^2)	Average Electric Field (V/m)
0.20	8.45×10^{11}	1371.53
0.25	1.25×10^{11}	2023.48
0.30	1.46×10^{11}	2362.85
0.35	1.50×10^{11}	2441.78
0.40	1.52×10^{11}	2468.90

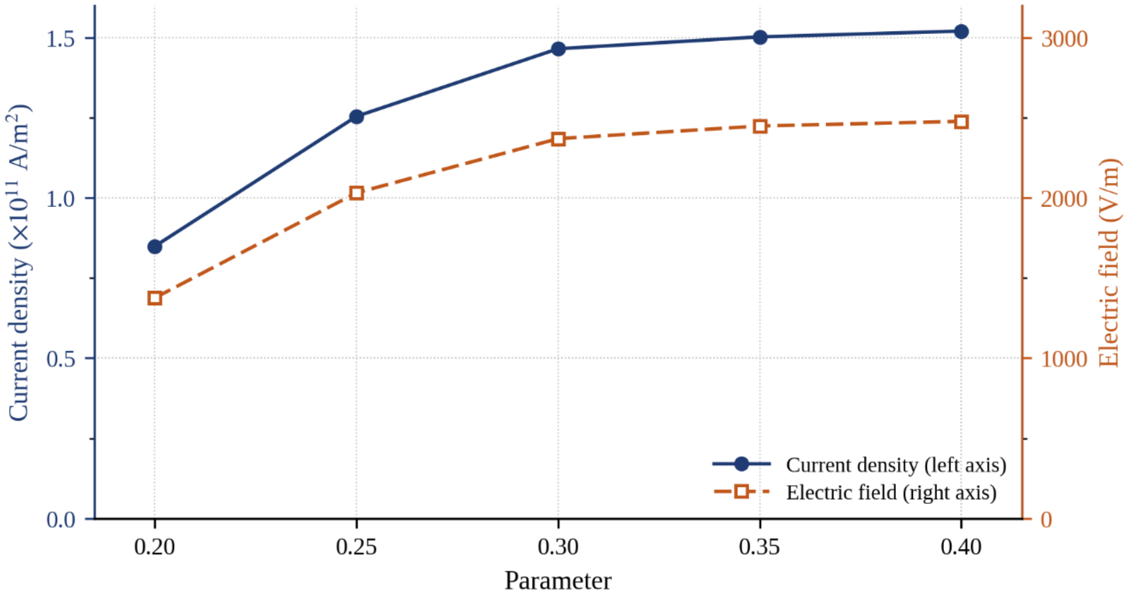

Figure 5. Graph of the average current density and electric field by varying the width of the fingers.

3.3. Dependence on the number of electrodes

Table 4 shows the simulation results for the distribution of current density and electric field magnitude for sensors with different numbers of fingers. Initially, the current density graph (Fig. 6) rose significantly from 4 to 8 electrodes. Regarding the number of fingers, it began at $1.78\ x\ 10^{10} A/m^2$ at 4 electrodes and then dramatically climbed to 8 electrodes before declining to $1.57\ x\ 10^{10} A/m^2$ at 12 electrodes. Thus, the current density is highest with 8 fingers. The graph in Fig. 6 illustrates the electric field increasing steadily between 4 and 8 electrodes, from about 288.67 V/m to 2581.52 V/m. Then, the graph dropped from 8 to 10 electrodes. After that, the number rose slightly to 1486.46 V/m at 12 electrodes. Thus, 8 electrodes recorded the highest electric field value, while 4 electrodes recorded the lowest.

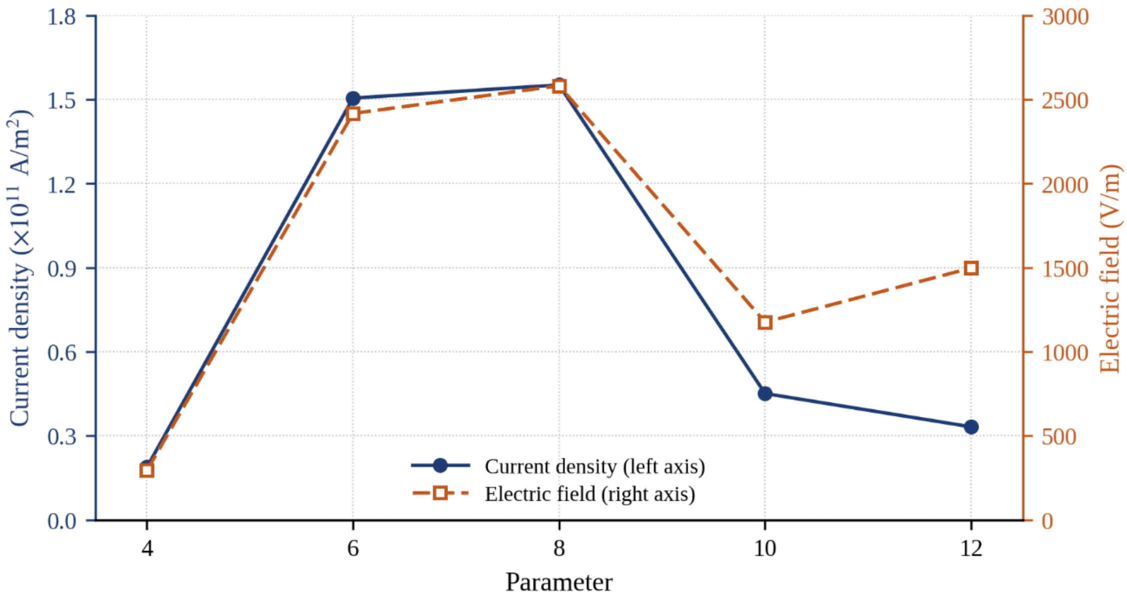

Figure 6. Graph of the average current density and electric field by varying the number of electrodes.

Table 4. The average current density for varying numbers of electrodes

Number of electrodes	Average Current Density (A/m^2)	Average Electric Field (V/m)
4	1.78 x 10^{10}	288.67
6	1.49x 10^{11}	2414.55
8	1.57 x 10^{11}	2581.52
10	4.41 x 10^{10}	1160.89
12	3.22 x 10^{10}	1486.46

3.4. Dependence on the Type of Material

The simulation results for silver, gold, and platinum electrodes show identical current density and electric field distributions, as shown in Fig. 7. Both the average current density and electric field (2581.52 V/m) are the same across all three materials. This outcome is expected because in steady-state electrostatic simulations, the electric field distribution is determined solely by electrode geometry and applied boundary conditions, not by intrinsic material properties [22]. Material conductivity influences current density magnitude only in more complex, time-dependent models.

These three electrode materials are widely used in sensing applications. Platinum offers the highest stability but is prohibitively expensive. Gold provides excellent stability and conductivity; however, its high cost limits practicality for disposable devices. Silver delivers comparable electrical performance at a significantly lower cost, making it the most economically viable choice.

Based on these findings, silver was selected as the optimal electrode material. Despite identical simulation results, silver provides the best balance of high conductivity, cost-effectiveness, and sufficient stability for electrochemical sensing applications. The simulation confirms no performance advantage from using gold or platinum. Therefore, silver was chosen to maximize device performance while maintaining practical economic feasibility for future commercialization.

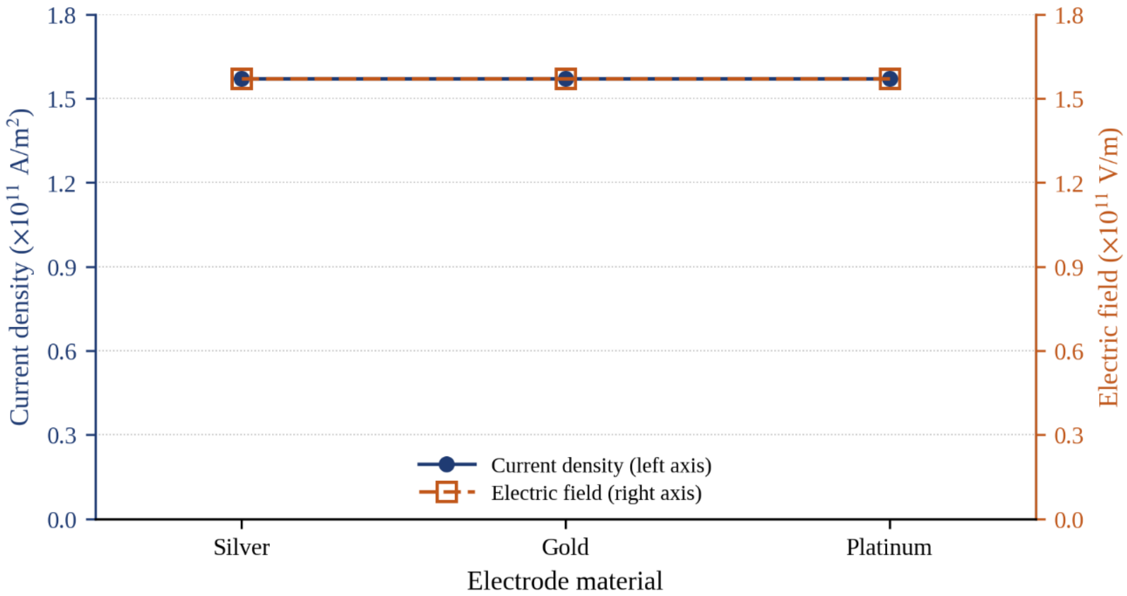

Figure 7. Graph of the average current density and electric field by varying the type of materials

https://doi.org/10.31436/iiumej.v27i3.3191

3.5. Experimental Result

All samples were tested at 1 kHz frequency for 5 hours via an LCR meter with a 1 V supply voltage. Fig. 8 shows the resistance of pure and commercialized fruit juices at 1 kHz. Commercialized apple juice exhibits the most significant resistance increase, rising from 16 Ω to 35 Ω, while commercialized orange juice increases modestly from 20 Ω to 23 Ω. Pure apple and orange juices maintain consistently low resistance values between 2.5 Ω and 6 Ω throughout the experiment. This divergence is attributed to compositional differences; commercial juices contain preservatives, added sugars, and stabilizers that alter ionic conductivity and undergo electrochemical degradation over time, causing resistance drift [23]. Pure juices, with natural composition and minimal additives, exhibit stable resistance profiles.

Deionized (DI) water was deliberately excluded from this experiment. DI water has extremely low ionic conductivity, resulting in resistance values that exceed the measurable range of the LCR meter. Even with 1 V excitation, the sensor would produce near-infinite resistance, rendering the graph unreadable and providing no meaningful comparative data. Moreover, DI water lacks the ionic species and organic compounds necessary for electrochemical interaction with the IDE electrodes, making it unsuitable as a reference medium for juice adulteration studies. The fabricated IDE sensor successfully distinguishes between pure and commercial juices based on their distinct resistance signatures, validating its potential for detecting adulteration in commercial fruit juice products.

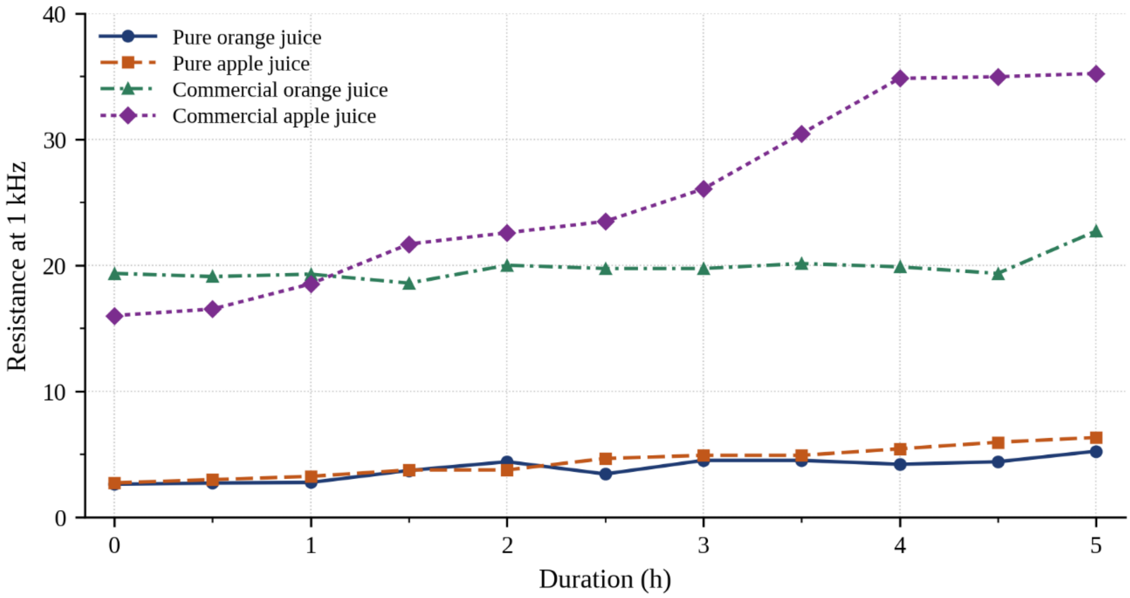

Figure 8. The resistance of pure and commercial fruit juices at 1kHz.

4. Conclusion

The electric field distribution was generated using an electrostatics study within the COMSOL AC/DC module for the interdigitated electrode (IDE) simulations. The primary objective of this simulation was to evaluate the influence of key design parameters—namely finger width, gap spacing, finger number, and electrode material—on the resulting electric field and current density distributions. As shown by the simulation results, smaller gap spacings and optimized finger widths produce significantly higher electric field intensities because potential gradients concentrate in confined regions. Therefore, systematically optimizing these geometric parameters can effectively maximize IDE performance for sensing applications.

Among the four parametric studies, finger width and gap spacing were the dominant factors influencing IDE performance, whereas the number of fingers and electrode material type had negligible effects on electric field magnitude. The optimal configuration, featuring a gap spacing of 0.1 mm, a finger width of 0.4 mm, and eight finger pairs, yielded the highest electric field (2582.52 V/m) and current density (1.57×10^{10} A/m²). This enhanced electric field and current density directly correlate with improved sensitivity, as stronger localized fields facilitate greater charge accumulation and redox current at the electrode-electrolyte interface, making this design highly suitable for sensitive electrochemical sensor platforms.

ACKNOWLEDGEMENT

The authors acknowledge funding from the Research Management Center, International Islamic University Malaysia. The authors are very grateful to IIUM for providing machining and testing facilities to carry out the experiments and for their valuable support in this research.

REFERENCES

[1] S. N. Hosseini et al., "Recent advances in CMOS electrochemical biosensor design for microbial monitoring: Review and design methodology," *IEEE Trans. Biomed. Circuits Syst.*, vol. 17, no. 4, pp. 123–135, Aug. 2023.

[2] J.-C. Lim, S. C. B. Gopinath, H. Krishnan, and S.-M. Tan, "Faradaic and non-faradaic depletions by anodic electrode corrosion with strong electrolytes on tautochrone curve interdigitated electrodes," *Sci. Direct*, vol. 123, pp. 45–56, 2024.

[3] A. K. Assaifan et al., "Roles of interdigitated electrode geometry in non-faradaic impedimetric biosensors," *J. Electrochem. Soc.*, vol. 171, no. 8, p. 087515, 2024.

[4] A. Hedayatipour et al., "CMOS based whole cell impedance sensing: Challenges and future outlook," *Biosens. Bioelectron.*, vol. 143, Art. no. 111600, Oct. 2019.

[5] M. Z. Iskandarani, "Analytical and numerical modeling of electric field in coplanar devices with neural predictor," *Taylor & Francis Online*, vol. 56, no. 2, pp. 89–102, 2025.

[6] T. Zhang et al., "A special two-working-electrode system: A summary of recent development in fabrication and application of interdigitated array electrodes," *Nanotechnology*, vol. 36, no. 13, p. 132001, 2025.

[7] T. Americo da Silva et al., "Application of a microfluidic electronic tongue based on impedance spectroscopy for coconut water analysis," *Food Res. Int.*, vol. 178, p. 113925, 2024.

[8] T. Zhang, Y. Jian, Z. Deng, W. Wu, and F. Liu, "A special two-working-electrode system: A summary of recent development in fabrication and application of interdigitated array electrodes," *Nanotechnology*, vol. 36, no. 13, p. 132001, 2025.

[9] Habboush, S., Rojas, S., Rodríguez, N., & Rivadeneyra, A. (2024). The Role of Interdigitated Electrodes in Printed and Flexible Electronics. *Sensors*, vol. 24, no. 9, 2717.

[10] B. Sarkar, M. T. Rahman, M. M. Rahman, S. Hossen, L. Zhenguo, and N. H. Bhuiyan, "Amplification of electrochemical signal by moving interdigitated electrode array for highly sensitive detection of Alzheimer's disease markers in blood," *Biosens. Bioelectron.*, vol. 269, p. 116939, 2025.

[11] Hashim, U., Rijal, S., Dhahi, Th. S., Afnan Uda, M. N., Uda, M. N. A., Adam, T., & Pamungkas, Y. "Surface-specific reactivity and ionic selectivity in aluminium interdigitated electrode platforms for advanced electronic sensing interfaces," *Results Eng.*, vol. 28, p. 107325, Dec. 2025.

[12] L. M. A. Melo et al., "Electrochemistry of the synthetic tryptamine 5-MeO-MiPT at glassy carbon and screen-printed electrodes: A rapid and simple screening method for application in forensic analysis," *Sens. Actuators B Chem.*, vol. 393, p. 134183, Oct. 2023.

[13] M. B. Kulkarni and S. Goel, "Recent advancements in finite element analysis of interdigitated electrode sensors: A review," *Sens. Actuators A Phys.*, vol. 345, p. 113823, 2022. doi: 10.1016/j.sna.2022.113823.

[14] M. F. Hossain, J. W. Park, and M. Kim, "Simulation and optimization of interdigitated electrode geometry for enhanced electrochemical biosensing performance using COMSOL Multiphysics," *J. Electrochem. Sci. Technol.*, vol. 14, no. 2, pp. 165–175, 2023. doi: 10.33961/jecst.2022.00845.

[15] P. Sharma and A. Kumar, "Finite element analysis of interdigitated capacitive sensors: Effect of electrode geometry on electric field distribution and sensitivity," *IEEE Sensors J.*, vol. 24, no. 8, pp. 11892–11901, Apr. 2024. doi: 10.1109/JSEN.2024.3365237.

[16] A. K. Assaifan, R. A. Almansour, J. A. Alessa, S. Alhudaithy, A. S. Fakhouri, and A. A. Alsaleh, "Roles of interdigitated electrode geometry in non-faradaic impedimetric biosensors," *J. Electrochem. Soc.*, vol. 171, no. 8, p. 087515, 2024. doi: 10.1149/1945-7111/ad6a99.

[17] A. K. Assaifan, R. A. Almansour, J. A. Alessa, A. Altinawi, and S. Alhudaithy, "Impact of interdigital electrode count on non-faradaic electrochemical biosensor performance for detecting pathogens associated with newborn disabilities," *J. Electrochem. Soc.*, vol. 172, no. 5, p. 057515, 2025. doi: 10.1149/1945-7111/addb85.

[18] COMSOL Multiphysics® v. 5.6 AC/DC Module User's Guide. Stockholm, Sweden: COMSOL AB, 2020.

[19] S. S. Deshpande, G. Bacher, and S. Bhand, "Design and Development of Micro Interdigitated Electrodes Devices for Sensitive and Reliable Biosensors," Ph.D. dissertation, Birla Institute of Technology and Science, Pilani, India, 2023.

[20] V. R. Naganaboina, S. Bonam, M. Anandkumar, A. S. Deshpande, and S. G. Singh, "Improved chemiresistor gas sensing response by optimizing the applied electric field and interdigitated electrode geometry," *Sensors Actuators A: Phys.*, 2023.

[21] J. Zhang, V. Selamneni, B. P. Yalagala, M. Amjadi, and H. Heidari, "Development of Dielectrophoresis Electrodes for Nanowire Alignment," *Eng. Proc.*, vol. 127, no. 1, p. 9, Mar. 2026, doi: 10.3390/engproc2026127009.

[22] F. Li, C. Zhou, and A. Klinkova, "Simulating electric field and current density in nanostructured electrocatalysts," *Phys. Chem. Chem. Phys.*, vol. 24, no. 42, pp. 25695–25719, Oct. 2022, doi: 10.1039/d2cp02846h.